272–281 *Nucleic Acids Research, 2015, Vol. 43, No. 1* *Published online 17 December 2014*
doi: 10.1093/nar/gku1300

Active destabilization of base pairs by a DNA glycosylase wedge initiates damage recognition

Nikita A. Kuznetsov[1,2,†], Christina Bergonzo[3,†], Arthur J. Campbell[3], Haoquan Li[3], Grigory V. Mechetin[1], Carlos de los Santos[4], Arthur P. Grollman[4], Olga S. Fedorova[1,2,*], Dmitry O. Zharkov[1,2,*] and Carlos Simmerling[3,5,*]

[1]SB RAS Institute of Chemical Biology and Fundamental Medicine, 8 Lavrentieva Ave., Novosibirsk 630090, Russia, [2]Department of Natural Sciences, Novosibirsk State University, 2 Pirogova St., Novosibirsk 630090, Russia, [3]Department of Chemistry, Stony Brook University, Stony Brook, NY 11794, USA, [4]Department of Pharmacological Sciences, Stony Brook University, Stony Brook, NY 11794, USA and [5]Laufer Center for Physical and Quantitative Biology, Stony Brook University, Stony Brook, NY 11794, USA

Received November 09, 2014; Revised November 26, 2014; Accepted November 28, 2014

ABSTRACT

Formamidopyrimidine-DNA glycosylase (Fpg) excises 8-oxoguanine (oxoG) from DNA but ignores normal guanine. We combined molecular dynamics simulation and stopped-flow kinetics with fluorescence detection to track the events in the recognition of oxoG by Fpg and its mutants with a key phenylalanine residue, which intercalates next to the damaged base, changed to either alanine (F110A) or fluorescent reporter tryptophan (F110W). Guanine was sampled by Fpg, as evident from the F110W stopped-flow traces, but less extensively than oxoG. The wedgeless F110A enzyme could bend DNA but failed to proceed further in oxoG recognition. Modeling of the base eversion with energy decomposition suggested that the wedge destabilizes the intrahelical base primarily through buckling both surrounding base pairs. Replacement of oxoG with abasic (AP) site rescued the activity, and calculations suggested that wedge insertion is not required for AP site destabilization and eversion. Our results suggest that Fpg, and possibly other DNA glycosylases, convert part of the binding energy into active destabilization of their substrates, using the energy differences between normal and damaged bases for fast substrate discrimination.

INTRODUCTION

How enzymes recognize their cognate substrates is a long-standing question in molecular biology. As a case in point, DNA repair enzymes efficiently discriminate between normal and damaged DNA, which often are quite similar in overall structure. For example, formamidopyrimidine-DNA glycosylase (Fpg) excises oxidized purines from DNA. Its substrates include 7,8-dihydro-8-oxoguanine (oxoG) and the formamidopyrimidine derivatives of guanine and adenine. The structural basis of DNA binding by Fpg from several bacterial species, including *Escherichia coli* (*Eco*-Fpg) and *Geobacillus stearothermophilus* (*Bst*-Fpg), has been revealed by X-ray crystallography (1–9) and molecular dynamics (MD) (6,7,10–16). As with other DNA glycosylases, complexity of substrate structure requires extensive conformational changes in DNA after binding to the enzyme to achieve a catalytically competent conformation. These changes include DNA kinking and eversion of the damaged dN from the helix into the lesion-binding pocket of the enzyme. Fpg also undergoes several conformational transitions, among them a possible closing movement of enzyme domains, insertion of several amino acid residues into the void vacated by the everted lesion and isomerization of the active site.

The kinetic scheme of oxoG excision by Fpg, studied by stopped-flow and quench-flow methods (17–22), reveals at least five reversible conformational transitions in the enzyme–substrate complex preceding one irreversible step of the reaction. As a result of this multistep conformational change in the enzyme and its substrate, Fpg discriminates very strongly in favor of oxoG and against undamaged G (17,18,21). Structural data suggest that most of the conformational change in the Fpg–DNA complex seems to be promoted by insertion of three critical residues: Phe, Arg and Met. The roles ascribed to these residues are that Phe wedges between the pair containing the damaged base and

*To whom correspondence should be addressed. Tel: +7 383 3635128; Fax: +7 383 3635153; Email: dzharkov@niboch.nsc.ru
Correspondence may also be addressed to Carlos Simmerling, Tel: +1 631 6321336; Fax: +1 631 6327960; Email: carlos.simmerling@stonybrook.edu
Correspondence may also be addressed to Olga S. Fedorova. Tel: +7 383 3635175; Fax: +7 383 3635153; Email: fedorova@niboch.nsc.ru
†These authors contributed equally to the paper as first authors.

© The Author(s) 2014. Published by Oxford University Press on behalf of Nucleic Acids Research.
This is an Open Access article distributed under the terms of the Creative Commons Attribution License (http://creativecommons.org/licenses/by-nc/4.0/), which permits non-commercial re-use, distribution, and reproduction in any medium, provided the original work is properly cited. For commercial re-use, please contact journals.permissions@oup.com

the base pair 3′ to it, Arg stabilizes the initial bound conformation of the complex and later competes for hydrogen bonding with the C opposite to the lesion and Met prevents the lesion, once everted, from falling back into the helix stack (5,7,9). However, the order of events in the Fpg–DNA complex during the encounter and sampling of damaged and normal bases, and the degree to which these events contribute to the enzyme's specificity, remain unclear.

High-quality atomistic simulation, based on available structures, is being used increasingly to analyze conformational changes in enzymes during their catalytic cycle (23). On the other hand, transient enzyme kinetics, supplemented with site-directed mutagenesis and substrate perturbation provides valuable experimental information on protein dynamics, but has low structural resolution (24). Combining atomistic simulation with kinetic experiments is a powerful tool that provides insights into the dynamic nature of substrate recognition and processing by enzymes. In this work, we have used such a combined approach to address the mechanism of DNA substrate interrogation by Fpg.

MATERIALS AND METHODS

Oligonucleotides and enzymes

Eco-Fpg was purified and assayed as described (18,19) to >98% purity; the fraction of the active enzyme was ∼90%. Site-directed mutants were constructed using the QuikChange kit (Stratagene), purified and analyzed in the same way. Oligonucleotides were synthesized from commercially available phosphoramidites (Glen Research), processed if necessary and purified as described (18).

Stopped-flow measurements

All experiments were carried out at 25°C in the buffer containing 50 mM Tris–HCl (pH 7.5), 50 mM KCl, 1 mM EDTA, 1 mM DTT and 9% glycerol (v/v). Stopped-flow measurements with fluorescence detection were carried out as described (18,19) using a model SX.18MV stopped-flow spectrometer (Applied Photophysics, UK). The dead time of the instrument was 1.38 ms. Trp fluorescence experiments were carried out with 1 μM Fpg and 0.5–4.0 μM ligand or substrate, while aPu and FRET experiments, with 1 μM ligand or substrate and 0.25–4.0 μM Fpg. The following excitation and emission wavelengths were used: $\lambda_{ex} = 293$ nm, $\lambda_{em} > 320$ nm (Schott filter WG 320, Schott, Mainz, Germany) for Trp fluorescence only; $\lambda_{ex} = 293$ nm, $\lambda_{em} = 335$–345 nm (Corion filter P10–340, Newport, Franklin, MA, USA) for Trp fluorescence with a simultaneous aPu fluorescence detection; $\lambda_{ex} = 310$ nm, $\lambda_{em} > 370$ nm (Corion filter LG-370) for aPu fluorescence; $\lambda_{ex} = 550$ nm, $\lambda_{em} > 645$ nm (Schott filter RG 645) for Cy3/Cy5 FRET; $\lambda_{ex} = 491$ nm, $\lambda_{em} > 530$ nm for fluorescein/DABCYL FRET. Each trace shown is an average of four or more individual experiments. Kinetic schemes and constants were obtained as described (17–19,22). Briefly, the data were corrected for bleaching using the equation:

$$F = (F_{obs} - F_{bkgd}) \times e^{k_b t} + F_{bkgd}$$

where F is the corrected fluorescence, F_{obs} is the observed fluorescence, F_{bkgd} is the background fluorescence, t is the time and k_b is the bleaching rate constant. For Trp measurements, the fluorescence was then corrected for inner filter effect due to absorption of the oligonucleotides at 293 nm using the equation:

$$F_c = F \times 10^{0.5 \times A_{293}}$$

where F_c is the fluorescence corrected for both bleaching and the inner filter, F is the fluorescence corrected for bleaching and A_{293} is the absorption at 293 nm. The corrected fluorescence was then described as a sum of fluorescences of individual species in the analyzed kinetic scheme, e.g. for Trp fluorescence and cleavable substrates (Schemes II and III):

$$F_c = f_0[E]_{free} + \sum_{i=1}^{n} f_i[ESi] + f_{n+1}[EP]$$

For other schemes or for DNA fluorophores, the equation was modified to include the appropriate species. Flux and mass ratio equations were included in the system (shown here for a productive reaction scheme with n reversible steps, e.g. Schemes II and III):

$$\frac{d[ES1]}{dt} = k_1[E]_{free}[S] + k_{-2}[ES2] - (k_{-1} + k_2)[ES1]$$

$$\frac{d[ESi]_{i\neq 1,n}}{dt} = k_i\,[ES(i-1)] + k_{-(i+1)}\,[ES(i+1)] - (k_{-i} + k_{i+1})[ESi]$$

$$\frac{d[ESn]}{dt} = k_n\,[ES(n-1)] - (k_{-n} - k_{n+1})[ES_n]$$

$$\frac{d[EP]}{dt} = k_{n+1}[ESn] + k_{-p}[E]_{free}[P] - k_p[EP]$$

$$[E]_0 = [E]_{free} + \sum_{i=1}^{n}[ESi] + [EP]$$

$$[S]_0 = [S] + \sum_{i=1}^{n}[ESi] + [EP] + [P]$$

For the reactions of non-cleavable ligand binding (e.g. Schemes I, IV and V), the system was modified accordingly to exclude the product formation step. The system was numerically integrated and fitted using DynaFit v4 software (25). For each type of experiments, several solutions with kinetic schemes containing different numbers of reversible steps preceding the irreversible step were obtained, and the goodness of fit was inspected using the scree test (26) as described earlier (19). The scheme was considered minimal when the number of reversible steps corresponded to the beginning of the shallow region of the SD versus number of steps graph.

Molecular dynamics

Simulations used the base eversion pathway described previously (16). Protein and DNA force fields were ff99SB (27)

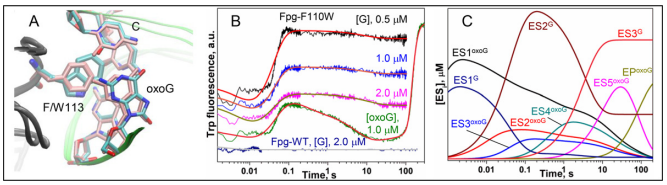

Figure 1. (**A**) Comparison of structure at the wedge insertion site for simulation structures of *Bst*-Fpg–DNA complex with Phe113 (pink) or Trp113 (colored by atom) wedge. (**B**) Experimental (jagged traces) and fit (smooth curves) time courses of Trp fluorescence during the interaction of *Eco*-Fpg-F110W and *Eco*-Fpg-WT with G-ligand (G:C) and oxoG-substrate (oxoG:C). A.u., arbitrary units. (**C**) Kinetic simulation of accumulation and disappearance of various enzyme–substrate complexes during the interaction of *Eco*-Fpg-F110W with undamaged (G-ligand) and damaged (oxoG-substrate) DNA.

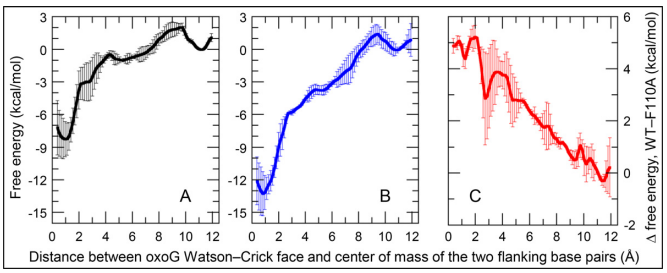

Figure 2. Comparison of free energy profiles for lesion eversion with Phe (**A**) and Ala (**B**) wedge. In each curve, the intrahelical position is on the left. Subtracting the profiles (**C**) shows that the mutation stabilizes the intrahelical state.

and parmbsc0 (28), respectively, with TIP3P explicit water (29) used in all simulations. The model system used for *Bst*-Fpg-WT/oxoG simulations was previously described elsewhere (16). The endpoint structures are based on coordinates from *Bst*-Fpg/DNA complexes with intrahelical G (2F5O; (4)) and fully everted oxoG (1R2Y; (3)). The sequence and residue numbering of DNA in the model is shown in Supplementary Figure S3 and Table S2, respectively. The parameters used in this work for oxoG were reported previously (16). AMBER parameters for the abasic site are included as Supplementary Files. The parameters were generated in two parts: charge fitting and atom-type assignment. The charges were generated from three alternate conformations and fit using the Restrained Electro-Static Potential (RESP) method (30). All other parameters and atom types were chosen through analogy.

Simulation details of abasic site

B-form DNA of sequence shown in Supplementary Figure S3B was built in AMBER nucgen. The central base was changed into an abasic site by deleting the base and using AMBER tleap to build in any missing atoms. Next the system was solvated with ∼8000 explicit solvent TIP3P water molecules in a truncated octahedron periodic box with an 8 Å buffer (29). Two consecutive rounds of minimization were run. The first round of minimization was run for 500 steps of steepest descent followed by 500 steps of conjugant gradient minimization while restraining all atoms in the DNA with a restraint force constant of 500.0 kcal/(mol·Å^2). In the second round of minimization, all restraints were removed and the minimization was run for 1000 steps of steepest descent followed by 1500 steps of conjugant gradient. The minimized structure was then run through two rounds of equilibration. In the first, the system was then heated to 330 K over the course of 20 ps while positional restraints of all atoms on the DNA were employed with a force constant of 10.0 kcal/(mol·Å^2). All bonds involving hydrogen were constrained using SHAKE and a time step of 2 fs was used (31). In the second round of equilibration, all restraints were removed and the system was allowed to relax for 100 ps. After equilibration, the system was simulated for 5 ns at 330 K and 1 atm. The last structure of this simulation is shown in Figure 3A.

Umbrella sampling

The goal of this work was to gauge the influence of the wedge in facilitating base eversion. Unlike our previous comprehensive comparison of major and minor groove pathways for complete eversion that required separately tracking base eversion and rotation around the glycosidic torsion (16), the process modeled here could be adequately described using a single reaction coordinate during umbrella sampling. We were able to simplify the calculation of the free energy by using the same structures mapping the NEB eversion pathway, but using only a distance measure for base pair opening (Supplementary Figure S5). We chose a subset of structure snapshots from the 2D umbrella sampling to use for the 1D calculation. To obtain these structures, and to confirm that the 1D distance metric adequately discriminated progress along the 2D surface, we drew a line connecting the intrahelical and extrahelical free energy minima (Supplementary Figure S6A). Shown in black dots overlaid on the surface are structures from the 2D umbrella sampling runs that were close to the connecting line and were therefore chosen for the 1D umbrella window initial coordinates. In Supplementary Figure S11B, we show that these structures chosen along the 2D path are nearly linear in progress along the 1D base pair distance variable that we used for 1D umbrella sampling. Overall, this demonstrates that the 1D representation adequately represents the progress in this region of our 2D free energy profile. The procedure described above provided initial structures for base pair opening in the wild-type (WT) system. For the wedge mutant, in each of these initial structures all atoms of the Phe side chain except CB were deleted, and tleap was used to add the H atoms on the Ala side chain. Each of the resulting F113A structures was equilibrated for 100 ps with a time step of 1 fs. During this equilibration, all heavy atoms of the DNA and Fpg were restrained with a restraint force constant of 100 kcal/(mol·Å^2), except the mutated residue 113 which was allowed to relax along with the solvent. During subsequent umbrella sampling, no restraints were used other than the reaction coordinate of base pair opening distance, which was the same as used for the WT system. The 1D distance reaction coordinate (Supplementary Figures S5 and S6) was calculated for each starting structure. Each structure was restrained to the closest 0.3 Å interval, yielding 40 windows along the distance reaction coordinate in 0.3 Å intervals from 0.3 Å to 12.0 Å. Each window was restrained to its respective grid point coordinates with a re-

straint force constant of 10 kcal/(mol·Å^2). Distance values corresponding to the reaction coordinate were written each time step for post-processing of free energy. Each window was simulated for 500 ps with a time step of 2 fs. The temperature of each window was held constant at 330 K using a Langevin thermostat with a Langevin collision frequency of 2.0 ps^{-1}, and the volume was held constant. An 8 Å nonbonded cutoff was applied to all windows. All bonds to hydrogen were constrained with SHAKE. After the umbrella sampling simulations were complete, the potential of mean force was extracted using the weighted histogram analysis method (32).

Simulation of the *Bst*-Fpg F113W mutant

To validate that Trp is a reasonable intercalating analog, we modeled the *Bst*-Fpg-F113W mutation in the *Bst*-Fpg-WT/oxoG system. After the last step of equilibration of the intrahelical oxoG bound to *Bst*-Fpg we converted Phe113 to Trp keeping the backbone and part of the aromatic ring to maintain the plane of the side chain. After the mutation we minimized the structure for 1000 steps of steepest descent followed by 20 ns of unrestrained dynamics under the same conditions outlined above for *Bst*-Fpg-WT/oxoG.

Simulations of intrahelical *Bst*-Fpg-WT/oxoG and *Bst*-Fpg-F113A/oxoG

Starting from the minimized, solvated and equilibrated intrahelical endpoints of *Bst*-Fpg-WT/oxoG and *Bst*-Fpg-F113A/oxoG, two sets of production dynamics were run for each system, with each simulation totaling ∼15 ns. Berendsen thermostat and barostat with 1 ps relaxation constants were used to perform simulations in the NPT ensemble at 1 atm and 330 K. SHAKE was used to constrain bonds to hydrogen, and a time step of 2 fs was employed. Different initial velocities were used to randomize trajectories. This provided 30 ns of total structure information for each of *Bst*-Fpg-WT/oxoG and *Bst*-Fpg-F113A/oxoG.

Energy decomposition

Molecular mechanics generalized Born surface area (MM-GBSA) in the Sander module of AMBER 12 was used to measure the energy decomposition, where idecomp was set to 2 or 4. The GB-OBC model (33) was used with an icosahedral surface area term (GBSA = 2 in AMBER), with a surface tension value of 0.005 kcal/(mol·Å^2). Per residue decomposition was performed on 50 frames each of the intrahelical window and the extrahelical site window (1.2 Å and 10.5 Å, respectively). The internal energy (idecomp = 2) of every residue (Supplementary Figure S10) was calculated and includes internal (bonds, angles, dihedrals), electrostatic, van der Waals and polar energies. The pairwise per-residue interaction energy (idecomp = 4) was measured for every residue to every other residue (Supplementary Figure S11). This included the internal (bonds, angles, dihedrals), electrostatic, van der Waals and polar energies.

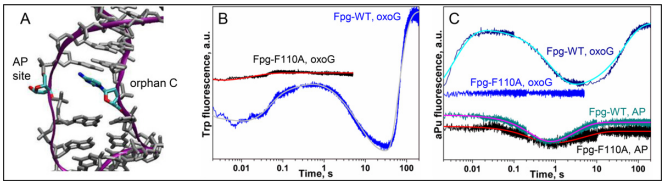

Figure 3. (**A**) Structure of duplex DNA containing a spontaneously everted AP site. (**B** and **C**) Experimental (jagged traces) and fitted (smooth curves) time courses of Trp (B) or aPu (C) fluorescence changes during cleavage of the oxoG:C (B and C) or AP substrates (C) by *Eco*-Fpg-WT and *Eco*-Fpg-F110A. A.u., arbitrary units.

RESULTS AND DISCUSSION

Choice of the experimental system

A combination of structural, modeling and high-resolution kinetic data provides a valuable instrument to dissect the mechanisms of enzyme activity and specificity. The widest and most useful set of Fpg structures comes from the *G. stearothermophilus* enzyme (2–9), a thermophilic species. On the other hand, biochemical and functional data overwhelmingly represent *Eco*-Fpg, and the high-temperature optimum of *Bst*-Fpg is challenging for a stopped-flow investigation of protein–DNA interactions. Therefore, crystallographic structures of *Bst*-Fpg were used as starting points for MD simulations, since these complexes, unlike the available structures of *Eco*-Fpg, contain the interrogated base. The complementary stopped-flow experiments were performed with *Eco*-Fpg, which has been extensively characterized, and for which the background stopped-flow data are available (17–22). All functionally important positions are conserved in both proteins (Supplementary Figure S1), suggesting that they use the same mechanism of damage base recognition and excision.

In complex with damaged DNA, both *Bst*-Fpg and *Eco*-Fpg wedge a Phe side chain (Phe110 in *Eco*-Fpg, Phe113 in *Bst*-Fpg; see Supplementary Figure S1 for the sequence alignment and numbering note) between the target base pair and the pair 3′ to the lesion. In addition, two side chains (Met and Arg) are inserted into the void generated by eversion of the damaged dN, and the axis of DNA is severely kinked (66°–75°) (1,2). Three groups of the *Bst*-Fpg structures represent pre-excision stages with the intact intercalating triad, one of an enzyme disulfide cross-link to undamaged DNA, another of Fpg with a disrupted active site cross-linked to oxoG-containing DNA before base eversion and the third of an E2Q catalytically inactive mutant in complex with oxoG-containing DNA following base eversion (3–5). In a complex with normal DNA, Phe113 is wedged into the duplex adjacent to the undamaged G:C pair, which is notably buckled, and the DNA is kinked, but eversion of the normal base is not observed. In contrast to these gross changes in DNA (and possibly protein) structure, stopped-flow analysis of *Eco*-Fpg binding undamaged DNA surprisingly reveals only a single kinetic stage in time course traces produced by fluorescence of the enzyme's native Trp residues, 2-aminopurine (aPu) or pyrrolocytosine reporter bases incorporated into the substrate (17–19,22). Detection of conformational transitions at early stages of

DNA binding could be hindered by a lack of fluorescent groups appropriately placed at the enzyme–DNA interface. On the other hand, it is not clear whether the 'insertion before eversion' structure (4) represents a true kinetic intermediate or is artificially stabilized by covalent enzyme–DNA cross-linking.

Fluorescence tracking of wedge insertion

To address the sequence of events preceding and following the insertion, we decided to construct an F110W mutant of *Eco*-Fpg, in which the fluorescent Trp residue substitutes for the Phe wedge, providing a suitable reporter at the Fpg–DNA interface. To analyze possible effects of the mutation on the structure of the *Eco*-Fpg–DNA recognition complex, we first built a model for intrahelical oxoG using the structure of *Bst*-Fpg bound to undamaged DNA. We then introduced *in silico* the corresponding F113W wedge mutation in the *Bst*-Fpg–DNA complex and performed a 20-ns MD simulation with both types of wedge. As shown in Figure 1A, replacement of the WT Phe phenyl wedge with the Trp indole has little effect on the DNA structure at the interrogation site, with the Trp wedge inserted slightly deeper than that of Phe. Relative to the crystal structure of *Bst*-Fpg cross-linked to undamaged DNA (PDB ID 2F5O), in simulations of both systems the root-mean-square deviation (RMSD) of the DNA fluctuated near 3 Å while that of the protein backbone remained near 1.5 Å (Supplementary Figure S2), suggesting that the mutation has little impact on the overall structure of the complex.

Having determined that replacing Phe with Trp in the Fpg–DNA complex was unlikely to affect its structure, we constructed the *Eco*-Fpg F110W mutant and investigated the steady-state and stopped-flow kinetics of its reaction with undamaged DNA (G-ligand), DNA containing an uncleavable abasic tetrahydrofuran moiety (THF), natural abasic site (AP) or oxoG opposite to C (Supplementary Figure S3). Steady-state K_M and k_{cat} of *Eco*-Fpg-F110W cleaving the oxoG-substrate were similar to those of *Eco*-Fpg-WT (Supplementary Table S1), supporting the results of the modeling. When the rate constants associated with pre-catalytic conformational adjustment and catalysis were measured by stopped-flow kinetics using the THF-ligand, AP- or oxoG-substrate (Supplementary Figure S4), the absolute values for different steps varied but the minimal reaction schemes remained the same as for *Eco*-Fpg-WT (Table 1, Schemes I–III in the Supplementary Material). No additional stages in the reaction scheme were revealed by introducing the Trp fluorophore, suggesting that, if a cognate lesion is present, conformational changes around the wedge coincide in time with those occurring in other Trp-containing parts of the Fpg molecule. Notably, the most pronounced changes in rate constants occurred at the stages presumed to involve substrate destabilization, wedge insertion and base eversion, processes most likely to be affected kinetically by the wedge mutation; the steps involved in primary binding (rate constants k_1 and k_{-1}) and late events that may correspond to product release and enzyme regeneration (k_5, k_{-5}, k_6) (20) were influenced to a much lesser extent.

The most drastic change was observed with the G-ligand, binding of which to *Eco*-Fpg-WT is described by a fast single-step equilibrium (characteristic time τ_1 ~5 ms) (17–19,22). The association of *Eco*-Fpg-F110W with this ligand could be separated into three fluorescently discernible stages, two of which clearly followed the fast binding (τ_2 ~50 ms, τ_3 ~10 s) (Figure 1B and C, Table 1, Scheme IV in the Supplementary Material). These changes in fluorescence most likely reflect conformational changes not observed in *Eco*-Fpg-WT due to lack of an appropriate fluorescent reporter at the DNA-binding interface. A comparison of the appearance and disappearance of different species during binding of the G-ligand and oxoG-substrate by *Eco*-Fpg-F110W (Figure 1C) suggests that the ES1 species in both Schemes III and IV are the same and characterize the primary encounter; Phe intercalation and base pair buckling likely occur at this stage as indicated by aPu fluorescence. ES2 in Scheme IV apparently corresponds to ES4 in Scheme III (22), the steps that reflect oxoG eversion and associated motions in the enzyme culminating in the *N*-glycosidic bond breakage when the base is damaged. Obviously, even if G can be everted from the DNA duplex, further excision does not occur, thus, at this stage, the processes of sampling of the normal and the damaged base must diverge. Finally, the ES3 species in Scheme IV may reflect a non-productive attempt of formation of the catalytically competent complex, since species ES5 in the productive scheme likely corresponds to post-catalytic events (20–22).

In the structures of undamaged DNA bound to *Bst*-Fpg, the Phe wedge causes significant buckling at the intercalation site, potentially probing the stability of the interrogated base pair (4); this buckling may correspond to one of the early fluorescence changes detected in our experiments. In any case, sampling of the normal G base by *Eco*-Fpg-F110W seems to be extensive and involve several conformational changes following insertion of the wedge. As similar reaction schemes are observed for other substrates and ligands processed by *Eco*-Fpg-WT and *Eco*-Fpg-F110W, one may expect that *Eco*-Fpg-WT also samples deeply the G base. In the structure of a *Bst*-Fpg-N173C disulfide cross-link to undamaged DNA, in which the DNA backbone is distorted artificially to stabilize the extrahelical G, the sampled base cannot enter the active site but, instead, is packed into the DNA minor groove (6). Structural studies with three other DNA glycosylases, human 8-oxoguanine-DNA glycosylase OGG1 (34,35), human uracil-DNA glycosylase (36) and *E. coli* alkylpurine-DNA glycosylase AlkA (37) suggest that extensive sampling of normal bases ending in a catalytically improper conformation of the enzyme–substrate complex may be a common theme in discrimination of normal bases from damaged ones.

Computational analysis of the role of the wedge in lesion processing

As the wedge insertion by Fpg could represent a critical step in initiating eversion from the helix of both undamaged and damaged dN, abolishment of this residue should make the eversion unfavorable. The F113A mutation in *Bst*-Fpg decreases the observed single-turnover k_{cat} by ~2 orders of

Table 1. Pre-steady-state parameters of *Eco*-Fpg WT and mutants; Trp fluorescence

	Eco-Fpg-WT[a]				*Eco*-Fpg-F110W[b]				*Eco*-Fpg-F110A[b]
	G	THF[c]	AP[d]	oxoG[e]	G[f]	THF[c]	AP[d]	oxoG[e]	oxoG[g]
k_1, $M^{-1}s^{-1}$	$(230 \pm 40) \times 10^6$	$(150 \pm 20) \times 10^6$	$(800 \pm 30) \times 10^6$	$(320 \pm 15) \times 10^6$	$(260 \pm 10) \times 10^6$	$(140 \pm 6) \times 10^6$	$(230 \pm 8) \times 10^6$	$(340 \pm 10) \times 10^6$	$(100 \pm 14) \times 10^6$
k_{-1}, s^{-1}	2700 ± 200	270 ± 15	250 ± 20	890 ± 25	1100 ± 90	920 ± 30	300 ± 40	700 ± 25	990 ± 250
k_2, s^{-1}		6.0 ± 0.2	36 ± 3	250 ± 18	50.6 ± 4.8	11.9 ± 1.3	13.1 ± 1.1	27.7 ± 1.4	54 ± 13
k_{-2}, s^{-1}		0.02 ± 0.005	65 ± 8	2.4 ± 0.4	1.8 ± 0.4	31.6 ± 1.8	39.4 ± 5.2	63 ± 2	40 ± 3
k_3, s^{-1}		10.0 ± 0.6	10.0 ± 0.5	6.7 ± 0.8	0.24 ± 0.05	7.1 ± 0.5	3.4 ± 0.1	22 ± 1	
k_{-3}, s^{-1}		0.6 ± 0.1	40 ± 4	46 ± 0.6	0.09 ± 0.01	1.71 ± 0.16	1.74 ± 0.08	28 ± 1	
k_4, s^{-1}		0.04 ± 0.007	11.0 ± 0.8	9.1 ± 0.6		0.26 ± 0.08	0.52 ± 0.01	4.5 ± 0.1	
k_{-4}, s^{-1}		0.01 ± 0.001	1.0 ± 0.1	2.4 ± 0.2		0.22 ± 0.04	0.03 ± 0.01	1.9 ± 0.1	
k_5, s^{-1}			0.20 ± 0.01	0.20 ± 0.01			0.30 ± 0.04	0.20 ± 0.01	
k_{-5}, s^{-1}				0.03 ± 0.007				0.02 ± 0.002	
k_6, s^{-1}				0.04 ± 0.006				0.021 ± 0.004	
K_P, M			$(1.8 \pm 0.3) \times 10^{-6}$	$(2.0 \pm 0.3) \times 10^{-6}$			$(0.5 \pm 0.1) \times 10^{-6}$	$(3.6 \pm 0.6) \times 10^{-6}$	

Estimate ± standard error of the estimate.
[a]From (18).
[b]This work.
[c]Scheme I (Supplementary Material).
[d]Scheme II (Supplementary Material).
[e]Scheme III (Supplementary Material).
[f]Scheme IV (Supplementary Material).
[g]Scheme V (Supplementary Material).

magnitude (9), and the same trend is observed for the *E. coli* enzyme (38). To understand the effect of the wedge on lesion sampling, we performed free energy calculations for oxoG eversion for *Bst*-Fpg-WT and for its F113A mutant with the wedge absent. We utilized the eversion pathway map that we previously published for Fpg (see (16) for an in-depth discussion of the major versus minor groove eversion pathway) to examine the impact of the wedge on the breaking of the interrogated base pair. Unlike in our previous work comparing major and minor groove eversion pathways, opening through the major groove could be well described by a single reaction coordinate, the distance between the center of mass of the Watson Crick face of the everting base and the center of mass of the two flanking base pairs (Supplementary Figures S5 and S6). The resulting free energy profiles for base pair opening by *Bst*-Fpg-WT and *Bst*-Fpg-F113A are shown in Figure 2. Essentially, the presence of Phe as the intercalating residue destabilized the intrahelical conformation but progressively less affected the further conformational intermediates. Intrahelical destabilization as the reason for the wedge effect was recently proposed based on the crystal structure of *Bst*-Fpg-F113A (9).

Eversion of oxoG in the WT enzyme was a predominantly low-barrier process in the simulations, encountering barriers of 5–7 kcal/mol. An experimental analysis of stepwise thermodynamics of oxoG recognition, binding and processing by *Eco*-Fpg-WT (22) also supports the low energy barrier of oxoG eversion. However, the final adjustment of Fpg–DNA complex into the catalytically competent conformation is highly unfavorable in enthalpy and is driven by favorable entropy increase (22), possibly due to a release of water molecules from the protein–DNA interface (4). In contrast, the barrier to breaking the oxoG:C base pair by *Bst*-Fpg-F113A during initial eversion (approaching 6 Å) was nearly 15 kcal/mol, much higher than for *Bst*-Fpg-WT. Since single molecule fluorescence experiments estimate the energetic barrier to 1D diffusion of *Bst*-Fpg along DNA at only ∼2 kcal/mol (39), it seems unlikely that the residence time of the enzyme at a particular interrogation site would be sufficient to overcome an eversion barrier that is more than 10 kcal/mol higher than that of translocation. Further supporting this conjecture, quantum dot-labeled single molecule fluorescence experiments show that *Eco*-Fpg-F110A shifts to faster 1D diffusion rates on DNA, indicating the wedge plays a direct role in the intrahelical base interrogation attributed to slower diffusion rate components (38).

Wedge deletion mutant lacks glycosylase function but retains AP lyase activity

Based on results of our computational modeling, an Fpg wedge mutant should be less competent at the stage of lesion eversion. We constructed the *Eco*-Fpg-F110A mutant and analyzed its activity on oxoG- and AP-substrates using steady-state and stopped-flow kinetics. Under steady-state conditions, the mutant enzyme was unable to process oxoG-substrates but maintained residual activity on AP-substrates (Supplementary Table S1), in line with observations that mutations of critical residues in Fpg and its homolog endonuclease VIII frequently abolish DNA glycosylase but not AP lyase activity (40–43).

When analyzed by the stopped-flow technique, interaction of *Eco*-Fpg-F110A with the oxoG-substrate could be described by two stages with kinetic parameters similar to the two initial steps observed for *Eco*-Fpg-WT (Table 1, Scheme V in the Supplementary Material); the reaction did not proceed further (Figure 3B). When aPu was incorporated 5′ or 3′ to the oxoG residue, *Eco*-Fpg-WT showed at least two conformational transitions preceding the irreversible step, while *Eco*-Fpg-F110A produced no changes (Figure 3C). As the fluorescence of aPu reflects the hydrophobicity of its environment (44), it may be inferred that no appreciable conformational transitions occur in DNA in the vicinity of the damaged base when *Eco*-Fpg-F110A binds its substrate. Consistent with the computational modeling, we conclude that *Eco*-Fpg-F110A forms a normal primary encounter complex with the oxoG-substrate, but fail-

Table 2. Pre-steady-state parameters of *Eco*-Fpg-WT and *Eco*-Fpg-F110A in binding and cleavage of the AP-substrate; aPu fluorescence

	Eco-Fpg-WT[a]	*Eco*-Fpg-F110A[a]
k_1, $M^{-1}\times s^{-1}$	$(9.7 \pm 0.4) \times 10^5$	$(3.6 \pm 0.5) \times 10^5$
k_{-1}, s^{-1}	1.7 ± 0.1	2.6 ± 0.6
k_2, s^{-1}	0.87 ± 0.07	0.50 ± 0.06
K_P, M	$(4.4 \pm 0.6) \times 10^{-6}$	$(3.3 \pm 0.6) \times 10^{-6}$

Estimate ± standard error of the estimate is shown.
[a]Scheme VI (Supplementary Material).

ure to insert a bulky wedge next to the damaged base precludes further reaction steps.

Reaction of *Eco*-Fpg-F110A with the AP-substrate also was visible by Trp fluorescence; however, rather small intensity changes rendered the signal-to-noise ratio low and quantification unreliable. Hence, we analyzed the AP substrate using aPu fluorescence, obtaining values for rate constants of individual conformational transitions that were similar for *Eco*-Fpg-WT and *Eco*-Fpg-F110A (Figure 3C, Table 2, Scheme VI in the Supplementary Material). In this case, changes in aPu fluorescence are likely due to intercalation of other plugging residues (Met73 and Arg108). The stopped-flow results agree with the steady-state activity of *Eco*-Fpg-F110A and with modeling that indicates relaxed requirements for wedge insertion in AP site cleavage.

To understand the residual activity for the AP-substrate, we performed a simulation for duplex DNA with an AP site replacing the oxoG. We observed that the AP substrate preferred the extrahelical position even in the absence of Fpg, due to rearrangement of the backbone that minimizes the gap resulting from lack of a base (Figure 3A). The eversion distance for the AP-substrate was stable near 12–15 Å (Supplementary Figure S7); thus, the model indicates that no wedge is required to facilitate eversion in this case. Combined, these evidence suggest that sampling barrier and Fpg residence time at the AP site would be less affected by an Phe-to-Ala mutation compared with the oxoG lesion; indeed, *Eco*-Fpg-F110A shows only a moderate change in the AP site cleavage processivity, a property that reflects both the 1D diffusion rate and the catalytic efficiency of the enzyme (45).

Finally, we followed the efficiency of Förster resonance energy transfer (FRET) in the stopped-flow mode to explore effects of the wedge mutation on the ability of Fpg to bend substrate DNA. The oxoG-substrate was modified at the opposite 5′-termini either with a pair of fluorescent dyes (Cy3 and Cy5), in which case the emission from Cy5 after photon transfer from Cy3 was monitored, or with a dye–quencher pair (fluorescein and DABCYL), so as to observe quenching of fluorescein emission. When the Cy3/Cy5 oxoG-substrate was cleaved by *Eco*-Fpg-WT, the Cy5 fluorescence initially increased and then started to decay (Figure 4A and B); the fluorescein emission from the fluorescein/DABCYL pair almost exactly mirrored inversely the Cy5 emission (Figure 4A). The data were optimally fit by Scheme VII (Supplementary Material), with rate constants presented in Table 3. The enzyme essentially overbends DNA during primary binding and initial conformational changes, then relaxes it. However, with the *Eco*-

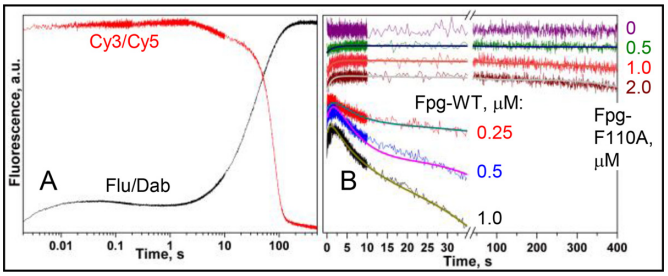

Figure 4. FRET time courses during cleavage of oxoG-substrate by Fpg. (**A**) Comparison of Cy3/Cy5 (red) and fluorescein/DABCYL time courses for *Eco*-Fpg-WT. (**B**) FRET time courses for *Eco*-Fpg-WT and *Eco*-Fpg-F110A. Jagged traces represent experimental data, smooth curves show the fit to Scheme VII (Supplementary Material). A.u., arbitrary units.

Table 3. Pre-steady-state parameters of *Eco*-Fpg-WT and *Eco*-Fpg-F110A in binding and cleavage of the oxoG-substrate; Cy3/Cy5 FRET

	Eco-Fpg-WT[a]	*Eco*-Fpg-F110A
k_1, $M^{-1}\times s^{-1}$	$(2.8 \pm 0.3) \times 10^5$	$(2.1 \pm 0.1) \times 10^5$
k_{-1}, s^{-1}	0.88 ± 0.04	0.58 ± 0.05
k_2, s^{-1}	0.35 ± 0.06	0.0023 ± 0.0001
k_{-2}, s^{-1}	0.0020 ± 0.0004	0.00035 ± 0.00004
k_3, s^{-1}	0.050 ± 0.010	n/c[b]
K_P, M	$(2.1 \pm 0.5) \times 10^{-6}$	n/c[b]

Estimate ± standard error of the estimate is shown.
[a]Scheme VII (Supplementary Material).
[b]n/c, not cleaved.

Fpg-F110A mutant, the Cy5 fluorescence decay was significantly prolonged (Figure 4B), suggesting that both enzymes quickly bend DNA but *Eco*-Fpg-F110A is much slower to proceed further, showing no appreciable cleavage of the substrate up to 400 s. Lack of appreciable aPu signal (see above) indicates that the mutant is able to bend DNA without significantly disrupting the stacking around oxoG.

How does the wedge destabilize the interrogated base pair?

The experimental data confirmed the role of the wedge, as suggested by the calculated free energy profiles for lesion eversion. Therefore, we performed further computational analyses to gain insight into the mechanism of lesion destabilization.

As noted above, the interrogated base pair and its 3′ GC base pair are significantly buckled in the structure of *Bst*-Fpg encountering an intrahelical G. Importantly, the two base pairs buckle in opposite directions, presumably coupled to wedge insertion. Our simulations reproduce this behavior for *Bst*-Fpg-WT interrogating oxoG, but in the *Bst*-Fpg-F113A wedge deletion mutant the base pairs remain buckled, but the values for two base pairs become nearly equivalent (structure snapshot shown in Figure 5A, with histograms in Supplementary Figure S8) allowing the bases to adopt almost canonical stacking geometries. This finding mirrors the observation in the structure of catalytically inactive *Bst*-Fpg-E2Q+F113A thiol-crosslinked to a G-containing DNA (9). The buckle induced by the wedge in the *Bst*-Fpg-WT structure implies weakening of stacking interactions between oxoG and its 3′ G neighbor. A shift in the

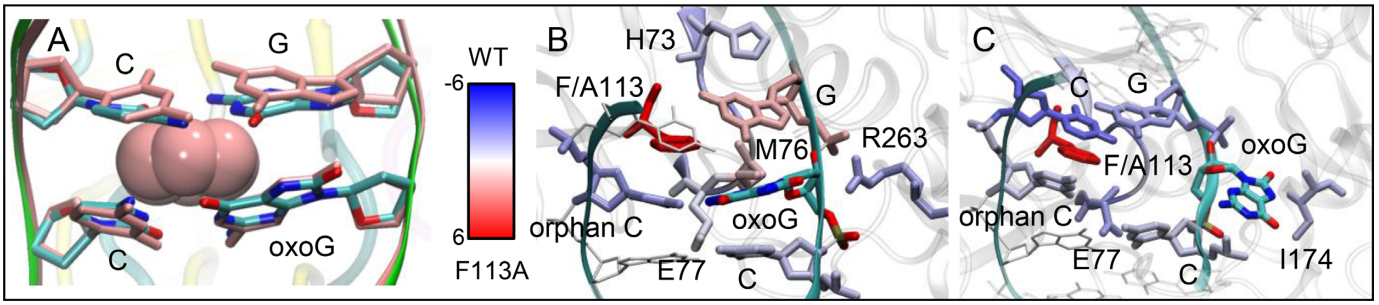

Figure 5. (**A**) Structure overlap at the interrogation site of *Bst*-Fpg-F113A (colored by atom) and *Bst*-Fpg-WT (pink). (**B** and **C**) Color-coded difference in interaction energies due to the wedge, mapped onto the WT intrahelical (B) and extrahelical average structures (C). The figure shows the difference in per residue energy decomposition between WT and F113A mutant. Positive (red) values reflect more favorable interactions in the mutant.

rise helicoidal parameter from the regular 3.6 Å to values above 4.5 Å (Supplementary Figure S9) further supports this hypothesis. Interestingly, the crystal structure of *Bst*-Fpg-E2Q+F113A thiol-crosslinked to an oxoG-substrate (9) shows an idosyncratic configuration of the damaged base, never observed in other Fpg structures: it is intrahelical but rotated into the *syn* orientation and disengaged from hydrogen bonding to the partner C. However, this structure most likely represents a global energy minimum where the complex settles after the long crystallization procedure with multiple cycles of DNA breathing and dissociation–reassociation events, whereas our F113A model is expected to reflect the structural and energetic features of the primary lesion encounter complex, and in this sense is more relevant to the lesion recognition process.

Both per residue and pair-wise decomposition of the total potential energy for structures sampled in the energy landscape minima, specifically at the intrahelical and extrahelical positions, were performed. We calculated the energy contribution of each residue to the system, mapping the difference in resulting values (WT–F113A) onto the average intrahelical and extrahelical WT structures (Figure 5B and C). The energy contribution of the G 3′ to the target oxoG base favors the mutant in the intrahelical location, reflecting the stability gained by removing the wedge, decreasing the buckling and improving base pair stacking. Residue 113 favors the mutant as well, illustrating the destabilizing role of this residue when it is Phe. Additionally, Met76 is allowed to shift away from the sugar–phosphate backbone in the mutant due to the gap created by loss of the wedge, improving its van der Waals energy and reducing electrostatic clashes. The third member of the gap-filling triad, Arg111, did not show a large energy effect on the stability of either extrahelical or intrahelical state.

We calculated the average interaction energy between each pair of residues for the *Bst*-Fpg-WT and *Bst*-Fpg-F113A mutant in the intrahelical and extrahelical locations (Supplementary Figures S10 and S11, respectively). Examination of the resulting data revealed that most interactions in the intrahelical location differ only slightly between the systems, and reflect small rearrangements and optimization of geometries in non-bonded interactions. This aggregation of many small energy improvements contributes to an overall stabilization of the mutant system intrahelical location. However, significant pairwise interactions which favor the WT system in the intrahelical and extrahelical position are specific to the eversion pathway. These pairs include an electrostatic interaction between oxoG and Arg263 in the intrahelical location, and stabilization of the 3′ base pair (282, 298) and the Met loop and catalytic loop regions (77, 222, 223) in the extrahelical position. Increased stabilization of the helix–two turn–helix DNA binding domain (156, 277) in the mutant intrahelical location may contribute to the slow unbending of DNA mentioned above.

The key effects of the wedge arise directly from oxoG buckling, and force the oxoG into a position in which further contacts along the base eversion pathway are stabilized, as shown in the energy decomposition. Conversely, the wedge mutant stabilization in the intrahelical location mainly arises from improved stacking, assisted by other non-specific pairwise interactions whose geometry is optimized from reduced spatial constraints. In the intrahelical state, Met76 is at the end of a strained loop region that undergoes a conformational change upon eversion, resulting in movement of Met76 into the minor groove and filling of the gap created by eversion of the lesion. Replacement of Met76 with Ala in *Bst*-Fpg promotes the same structure as do mutations in the loop binding the everted base, thus Met76 likely stabilizes the extrahelical state rather than destabilizes the intrahelical one (9). In the absence of the bulky wedge in *Bst*-Fpg-F113A, the intrahelical state undergoes steric repacking that allows the loop to relax prior to eversion, forming a favorable interaction with its surrounding residues, including the catalytic loop, intercalating Arg111 and the G base 3′ to oxoG (Figure 5B). The additional space also results in less effective gap filling by Met76 in the F113A everted state, shown by the shift in pairwise interaction energies toward favoring the WT. The overall effect is a significant stabilization of the intrahelical oxoG, contributing to the inability of the mutant Fpg to evert and process the lesion.

In conclusion, we have combined high-quality MD and stopped-flow kinetics with fluorescence detection to analyze a critical conformational change in the complex reaction catalyzed by formamidopyrimidine-DNA glycosylase. Our results suggest that, during lesion search, Fpg likely samples undamaged bases by wedge insertion and undergoes several conformational changes in the enzyme–DNA complex. A similar scheme was proposed for uracil-DNA glycosylase based on structural data (9). The strained conformation of

kinked DNA after Fpg binding may provide a source of energy for catalysis; however, the productive reaction must be triggered by wedge insertion, which therefore represents a critical step in the lesion recognition process. The wedge actively destabilizes the lesion through a buckling process that weakens the Watson–Crick hydrogen bonds and reduces 3′ stacking. This mechanism may be common for DNA glycosylases that possess an aromatic intercalating wedge (41,46–48).

SUPPLEMENTARY DATA

Supplementary Data are available at NAR Online.

ACKNOWLEDGEMENT

We acknowledge assistance with data analysis from Kun Song and Lin Fu (Stony Brook University).

FUNDING

National Cancer Institute [CA017395–33 to A.P.G.]; National Science Foundation [0549370 to C.B.]; Russian Foundation for Basic Research [13–04–00013 to O.S.F., 14–04–01879 to D.O.Z.]; Presidium of the Russian Academy of Sciences [MKB 6.11 to O.S.F., MKB 6.12 to D.O.Z.]. Part of the work with aPu and FRET experiments was specifically funded by Russian Science Foundation [14–24–00093 to D.O.Z.]. Part of the work with Trp stopped-flow experiments was specifically funded by Russian Science Foundation [14–14–00063 to N.A.K.]. NSF Teragrid [MCA02N028 to C.S.]. Funding for open access charge: Novosibirsk State University.
Conflict of interest statement. None declared.

REFERENCES

1. Gilboa,R., Zharkov,D.O., Golan,G., Fernandes,A.S., Gerchman,S.E., Matz,E., Kycia,J.H., Grollman,A.P. and Shoham,G. (2002) Structure of formamidopyrimidine-DNA glycosylase covalently complexed to DNA. *J. Biol. Chem.*, **277**, 19811–19816.
2. Fromme,J.C. and Verdine,G.L. (2002) Structural insights into lesion recognition and repair by the bacterial 8-oxoguanine DNA glycosylase MutM. *Nat. Struct. Biol.*, **9**, 544–552.
3. Fromme,J.C. and Verdine,G.L. (2003) DNA lesion recognition by the bacterial repair enzyme MutM. *J. Biol. Chem.*, **278**, 51543–51548.
4. Banerjee,A., Santos,W.L. and Verdine,G.L. (2006) Structure of a DNA glycosylase searching for lesions. *Science*, **311**, 1153–1157.
5. Qi,Y., Spong,M.C., Nam,K., Banerjee,A., Jiralerspong,S., Karplus,M. and Verdine,G.L. (2009) Encounter and extrusion of an intrahelical lesion by a DNA repair enzyme. *Nature*, **462**, 762–766.
6. Qi,Y., Spong,M.C., Nam,K., Karplus,M. and Verdine,G.L. (2010) Entrapment and structure of an extrahelical guanine attempting to enter the active site of a bacterial DNA glycosylase, MutM. *J. Biol. Chem.*, **285**, 1468–1478.
7. Qi,Y., Nam,K., Spong,M.C., Banerjee,A., Sung,R.-J., Zhang,M., Karplus,M. and Verdine,G.L. (2012) Strandwise translocation of a DNA glycosylase on undamaged DNA. *Proc. Natl Acad. Sci. U.S.A.*, **109**, 1086–1091.
8. Sung,R.-J., Zhang,M., Qi,Y. and Verdine,G.L. (2012) Sequence-dependent structural variation in DNA undergoing intrahelical inspection by the DNA glycosylase MutM. *J. Biol. Chem.*, **287**, 18044–18054.
9. Sung,R.-J., Zhang,M., Qi,Y. and Verdine,G.L. (2013) Structural and biochemical analysis of DNA helix invasion by the bacterial 8-oxoguanine DNA glycosylase MutM. *J. Biol. Chem.*, **288**, 10012–10023.
10. Amara,P., Serre,L., Castaing,B. and Thomas,A. (2004) Insights into the DNA repair process by the formamidopyrimidine-DNA glycosylase investigated by molecular dynamics. *Protein Sci.*, **13**, 2009–2021.
11. Perlow-Poehnelt,R.A., Zharkov,D.O., Grollman,A.P. and Broyde,S. (2004) Substrate discrimination by formamidopyrimidine-DNA glycosylase: distinguishing interactions within the active site. *Biochemistry*, **43**, 16092–16105.
12. Amara,P. and Serre,L. (2006) Functional flexibility of *Bacillus stearothermophilus* formamidopyrimidine DNA-glycosylase. *DNA Repair*, **5**, 947–958.
13. Song,K., Hornak,V., de los Santos,C., Grollman,A.P. and Simmerling,C. (2006) Computational analysis of the mode of binding of 8-oxoguanine to formamidopyrimidine-DNA glycosylase. *Biochemistry*, **45**, 10886–10894.
14. Song,K., Kelso,C., de los Santos,C., Grollman,A.P. and Simmerling,C. (2007) Molecular simulations reveal a common binding mode for glycosylase binding of oxidatively damaged DNA lesions. *J. Am. Chem. Soc.*, **129**, 14536–14537.
15. Nam,K., Verdine,G.L. and Karplus,M. (2009) Analysis of an anomalous mutant of MutM DNA glycosylase leads to new insights into the catalytic mechanism. *J. Am. Chem. Soc.*, **131**, 18208–18209.
16. Bergonzo,C., Campbell,A.J., de los Santos,C., Grollman,A.P. and Simmerling,C. (2011) Energetic preference of 8-oxoG eversion pathways in a DNA glycosylase. *J. Am. Chem. Soc.*, **133**, 14504–14506.
17. Fedorova,O.S., Nevinsky,G.A., Koval,V.V., Ishchenko,A.A., Vasilenko,N.L. and Douglas,K.T. (2002) Stopped-flow kinetic studies of the interaction between *Escherichia coli* Fpg protein and DNA substrates. *Biochemistry*, **41**, 1520–1528.
18. Koval,V.V., Kuznetsov,N.A., Zharkov,D.O., Ishchenko,A.A., Douglas,K.T., Nevinsky,G.A. and Fedorova,O.S. (2004) Pre-steady-state kinetics shows differences in processing of various DNA lesions by *Escherichia coli* formamidopyrimidine-DNA glycosylase. *Nucleic Acids Res.*, **32**, 926–935.
19. Kuznetsov,N.A., Koval,V.V., Zharkov,D.O., Vorobjev,Y.N., Nevinsky,G.A., Douglas,K.T. and Fedorova,O.S. (2007) Pre-steady-state kinetic study of substrate specificity of *Escherichia coli* formamidopyrimidine-DNA glycosylase. *Biochemistry*, **46**, 424–435.
20. Kuznetsov,N.A., Zharkov,D.O., Koval,V.V., Buckle,M. and Fedorova,O.S. (2009) Reversible chemical step and rate-limiting enzyme regeneration in the reaction catalyzed by formamidopyrimidine-DNA-glycosylase. *Biochemistry*, **48**, 11335–11343.
21. Koval,V.V., Kuznetsov,N.A., Ishchenko,A.A., Saparbaev,M.K. and Fedorova,O.S. (2010) Real-time studies of conformational dynamics of the repair enzyme *E. coli* formamidopyrimidine-DNA glycosylase and its DNA complexes during catalytic cycle. *Mutat. Res.*, **685**, 3–10.
22. Kuznetsov,N.A., Vorobjev,Y.N., Krasnoperov,L.N. and Fedorova,O.S. (2012) Thermodynamics of the multi-stage DNA lesion recognition and repair by formamidopyrimidine-DNA glycosylase using pyrrolocytosine fluorescence–stopped-flow pre-steady-state kinetics. *Nucleic Acids Res.*, **40**, 7384–7392.
23. Adcock,S.A. and McCammon,J.A. (2006) Molecular dynamics: survey of methods for simulating the activity of proteins. *Chem. Rev.*, **106**, 1589–1615.
24. Fisher,H.F. (2005) Transient-state kinetic approach to mechanisms of enzymatic catalysis. *Acc. Chem. Res.*, **38**, 157–166.
25. Kuzmic,P. (1996) Program DYNAFIT for the analysis of enzyme kinetic data: application to HIV proteinase. *Anal. Biochem.*, **237**, 260–273.
26. Cattell,R.B. (1966) The scree test for the number of factors. *Multivariate Behav. Res.*, **1**, 245–276.
27. Hornak,V., Abel,R., Okur,A., Strockbine,B., Roitberg,A. and Simmerling,C. (2006) Comparison of multiple Amber force fields and development of improved protein backbone parameters. *Proteins*, **65**, 712–725.
28. Pérez,A., Marchán,I., Svozil,D., Sponer,J., Cheatham,T.E. III, Laughton,C.A. and Orozco,M. (2007) Refinement of the AMBER force field for nucleic acids: improving the description of α/γ conformers. *Biophys. J.*, **92**, 3817–3829.

29. Jorgensen,W.L., Chandrasekhar,J., Madura,J.D., Impey,R.W. and Klein,M.L. (1983) Comparison of simple potential functions for simulating liquid water. *J. Chem. Phys.*, **79**, 926–935.
30. Cieplak,P., Cornell,W.D., Bayly,C. and Kollman,P.A. (1995) Application of the multimolecule and multiconformational RESP methodology to biopolymers: charge derivation for DNA, RNA, and proteins. *J. Comput. Chem.*, **16**, 1357–1377.
31. Ryckaert,J.-P., Ciccotti,G. and Berendsen,H.J.C. (1977) Numerical integration of the Cartesian equations of motion of a system with constraints: molecular dynamics of *n*-alkanes. *J. Comput. Phys.*, **23**, 327–341.
32. Kumar,S., Rosenberg,J.M., Bouzida,D., Swendsen,R.H. and Kollman,P.A. (1995) Multidimensional free-energy calculations using the weighted histogram analysis method. *J. Comput. Chem.*, **16**, 1339–1350.
33. Onufriev,A., Bashford,D. and Case,D.A. (2004) Exploring protein native states and large-scale conformational changes with a modified Generalized Born model. *Proteins*, **55**, 383–394.
34. Banerjee,A., Yang,W., Karplus,M. and Verdine,G.L. (2005) Structure of a repair enzyme interrogating undamaged DNA elucidates recognition of damaged DNA. *Nature*, **434**, 612–618.
35. Radom,C.T., Banerjee,A. and Verdine,G.L. (2007) Structural characterization of human 8-oxoguanine DNA glycosylase variants bearing active site mutations. *J. Biol. Chem.*, **282**, 9182–9194.
36. Parker,J.B., Bianchet,M.A., Krosky,D.J., Friedman,J.I., Amzel,L.M. and Stivers,J.T. (2007) Enzymatic capture of an extrahelical thymine in the search for uracil in DNA. *Nature*, **449**, 433–437.
37. Bowman,B.R., Lee,S., Wang,S. and Verdine,G.L. (2010) Structure of *Escherichia coli* AlkA in complex with undamaged DNA. *J. Biol. Chem.*, **285**, 35783–35791.
38. Dunn,A.R., Kad,N.M., Nelson,S.R., Warshaw,D.M. and Wallace,S.S. (2011) Single Qdot-labeled glycosylase molecules use a wedge amino acid to probe for lesions while scanning along DNA. *Nucleic Acids Res.*, **39**, 7487–7498.
39. Blainey,P.C., van Oijen,A.M., Banerjee,A., Verdine,G.L. and Xie,X.S. (2006) A base-excision DNA-repair protein finds intrahelical lesion bases by fast sliding in contact with DNA. *Proc. Natl Acad. Sci. U.S.A.*, **103**, 5752–5757.
40. Lavrukhin,O.V. and Lloyd,R.S. (2000) Involvement of phylogenetically conserved acidic amino acid residues in catalysis by an oxidative DNA damage enzyme formamidopyrimidine glycosylase. *Biochemistry*, **39**, 15266–15271.
41. Zharkov,D.O., Golan,G., Gilboa,R., Fernandes,A.S., Gerchman,S.E., Kycia,J.H., Rieger,R.A., Grollman,A.P. and Shoham,G. (2002) Structural analysis of an *Escherichia coli* endonuclease VIII covalent reaction intermediate. *EMBO J.*, **21**, 789–800.
42. Burgess,S., Jaruga,P., Dodson,M.L., Dizdaroglu,M. and Lloyd,R.S. (2002) Determination of active site residues in *Escherichia coli* endonuclease VIII. *J. Biol. Chem.*, **277**, 2938–2944.
43. Kropachev,K.Y., Zharkov,D.O. and Grollman,A.P. (2006) Catalytic mechanism of *Escherichia coli* endonuclease VIII: roles of the intercalation loop and the zinc finger. *Biochemistry*, **45**, 12039–12049.
44. Rachofsky,E.L., Osman,R. and Ross,J.B.A. (2001) Probing structure and dynamics of DNA with 2-aminopurine: effects of local environment on fluorescence. *Biochemistry*, **40**, 946–956.
45. Sidorenko,V.S. and Zharkov,D.O. (2008) Correlated cleavage of damaged DNA by bacterial and human 8-oxoguanine-DNA glycosylases. *Biochemistry*, **47**, 8970–8976.
46. Lau,A.Y., Wyatt,M.D., Glassner,B.J., Samson,L.D. and Ellenberger,T. (2000) Molecular basis for discriminating between normal and damaged bases by the human alkyladenine glycosylase, AAG. *Proc. Natl Acad. Sci. U.S.A.*, **97**, 13573–13578.
47. Bruner,S.D., Norman,D.P.G. and Verdine,G.L. (2000) Structural basis for recognition and repair of the endogenous mutagen 8-oxoguanine in DNA. *Nature*, **403**, 859–866.
48. Fromme,J.C., Banerjee,A., Huang,S.J. and Verdine,G.L. (2004) Structural basis for removal of adenine mispaired with 8-oxoguanine by MutY adenine DNA glycosylase. *Nature*, **427**, 652–656.